International Journal for Numerical Methods in Fluids

WILEY

RESEARCH ARTICLE OPEN ACCESS

Effect of Microchannel Geometry on Nanoparticle Deposition in Nanofluid Flow

Meng Wang[1,2] | Kai Zhang[1,3] | Juanli Zhang[2] | Jay Wang[4]

[1]Systems, Power & Energy Research Division, James Watt School of Engineering, University of Glasgow, Glasgow, UK | [2]Key Laboratory for Thermal Science and Power Engineering of Ministry of Education, Department of Energy and Power Engineering, Tsinghua University, Beijing, China | [3]Wuhan NARI Limited Liability Company of State Grid Electric Power Research Institute, Wuhan, Hubei, China | [4]School of Engineering, Computer & Mathematical Sciences, Auckland University of Technology (AUT), Auckland, New Zealand

Correspondence: Jay Wang (jay.wang@aut.ac.nz)

Received: 3 October 2025 | **Revised:** 15 June 2026 | **Accepted:** 4 August 2026

Keywords: discrete phase model | microchannel cooling | nanofluid | nanoparticle deposition

ABSTRACT

Particle deposition poses a significant challenge in the application of nanofluids within microchannels. This study provides an angle- and radius-resolved numerical analysis of nanoparticle deposition in bent microchannels and clarifies how microchannel geometry regulates deposition through curvature-induced acceleration, secondary flow, and particle-wall encounter mechanisms. The results demonstrate that the particle deposition number per unit area decreases from 28.612 to 8.941 as the bending angle increases from 30° to 120°. Furthermore, particle deposition per unit area decreases from 11.922 to 4.769 as the bending radius increases from 0.2 mm to 0.4 mm. The inlet and curved segments exhibit significantly higher particle deposition than the other segments. Specifically, deposition in the inlet segment is approximately 10 times higher than that in the other segments, while deposition in the curved segment is approximately three times higher. The Reynolds number and Dean number are identified as critical parameters for linking primary flow, curvature-induced secondary vortices, and deposition risk. These findings provide quantitative insights and a mechanistic framework for the rational design and optimization of nanofluid microchannel cooling systems.

1 | Introduction

Modern thermal management solutions increasingly incorporate microchannel cooling systems, particularly in applications with high heat flux, such as electronics, lasers, and aircraft components [1]. These systems employ microchannels with submillimetre widths (typically less than 1 mm) to circulate coolant in close proximity to heat sources, thereby enabling efficient heat removal. The enhanced performance primarily arises from the high surface-to-volume ratio of microchannels, which significantly improves convective heat transfer [2]. The development of nanofluids, engineered colloidal suspensions of nanoparticles in base fluids, has further advanced microchannel cooling technologies [3]. Nanoparticles are typically composed of metals or metal oxides and possess thermal conductivities significantly higher than that of the base fluid. As a result, they can markedly enhance both the thermal conductivity and convective heat transfer coefficient of nanofluids [4]. In addition, the presence of nanoparticles disrupts the thermal boundary layer, thereby further improving heat transfer efficiency [5].

Despite these advantages, the application of nanofluids introduces a critical challenge: nanoparticle deposition within microchannels [6]. Deposition, defined as the accumulation of

Abbreviations: CFD, computational fluid dynamics; DPM, discrete phase model.

particles on solid surfaces, represents a major bottleneck in the design and operation of nanofluid-based microchannel systems. Due to the confined geometry, nanoparticles are more likely to interact with channel walls, promoting deposition. Over time, such accumulation can result in channel blockage, reduced flow rates, and degradation of thermal performance [7]. Fouling is a tricky problem to solve. Fouling layers cause local constrictions that affect flow velocity and increase pressure drop. There may be maldistributions or even completely blocked microchannels in multichannel apparatuses, such as heat exchangers. Because of this phenomenon, all related industries suffer high financial losses as a result of increased costs associated with design, transportation, installation, and maintenance. For example, heat exchangers are oversized by 30% in order to prevent clogging [8]. Aside from requiring a high capital investment, this is also unfriendly to the environment due to the additional refrigerant charge. Even though fouling has been considered a major obstacle to the implementation of micro-devices, there are few methods available for its solution [9, 10]. Therefore, understanding and mitigating deposition behavior is essential to ensure long-term system reliability while fully exploiting the benefits of nanofluids.

Nanoparticle deposition in nanofluid-microchannel systems can be mitigated through optimization of microchannel geometry. While extensive efforts have been devoted to understanding thermophysical properties and transport mechanisms, the role of microchannel geometry in nanoparticle deposition remains comparatively underexplored [11]. Geometry not only dictates heat transfer performance through channel dimensions and layout, but also governs internal flow structures, which directly influence nanoparticle transport and deposition behavior. This interplay is crucial for mitigating fouling and maintaining long-term efficiency. For instance, geometric features such as curvature can induce secondary flows (e.g., Dean vortices), enhancing particle mixing and heat transfer, albeit often at the cost of increased pressure drop [12]. Kim et al. [13] developed a critical shear stress threshold model to predict clogging, showing that deposition occurs progressively and can ultimately lead to blockage. In addition, Li and Ahmadi [14] established widely accepted theoretical models for particle dispersion and deposition in turbulent microchannel flows, while Williams et al. [15] reported a nonlinear relationship between nanoparticle concentration and heat transfer enhancement, with optimal performance observed at intermediate concentrations.

Although these studies have identified key governing parameters of particle deposition such as fluid velocity, channel dimensions, particle size, and fluid properties, real systems involving bend and elbow sections are more complex [16]. In particular, nonlinear and angular microchannel configurations introduce complex flow patterns that alter velocity distributions, pressure gradients, and wall shear stresses, thereby significantly affecting nanoparticle transport and deposition [17]. However, the underlying mechanisms and thermal implications associated with these geometries remain insufficiently understood. Systematic investigations are therefore required to quantify the influence of geometric parameters on nanoparticle deposition, such as channel angle, curvature, and surface characteristics. A thorough understanding of these interactions is crucial for optimizing microchannel design and minimizing particle deposition.

Currently, the majority of studies have investigated particle deposition within straight or 90° bend channels, and have predominantly considered larger particles in macroscale systems. In contrast, investigations of nanoparticle transport in microchannels with varying geometrical configurations remain scarce. To address this gap, this article provides a systematic analysis of the influence of bend angles on particle deposition, alongside comparisons of nanoparticle flow at different curvature radii. A Discrete Phase Model (DPM) is employed to capture particle dynamics and deposition behavior under different geometric conditions. Furthermore, strategies for enhancing nanofluid stability and mitigating particle deposition are explored, with the aim of informing the design of more efficient and reliable microchannel cooling systems.

The remainder of this paper is organized as follows. Section 2 describes the microchannel geometries, governing particle-transport model, simulation assumptions, boundary conditions, DPM settings, grid sensitivity test, and validation strategy. Section 3 presents the effects of bending angle and curvature radius on velocity distribution, secondary flow, particle trajectories, deposition locations, and dimensionless deposition interpretation. Section 4 summarizes the principal findings, limitations, and implications for microchannel cooling design.

2 | Numerical Methods

As opposed to conventional thermofluids, nanofluids contain suspended metallic and nonmetallic particles at the nanoscale. In nanofluids, nanoparticles are dispersed in a base solution through physical or chemical methods typically at volume concentrations below 10% [18]. The discrete phase model (DPM) is the most appropriate simulation method for nanofluids. Particle deposition is commonly studied using a DPM [19]. The methodology adopted in this study is critical for understanding how angular variations and flow velocity influence nanoparticle deposition in microchannels. The systematic approach applied to ANSYS Fluent 2020 R2 simulations ensures an accurate and relevant investigation of these factors. The process encompasses microchannel geometry, fluid properties, flow conditions, physical models, and simulation parameters. The specific DPM methodology has already been discussed in our previous work, so only a brief description is provided here [20, 21].

2.1 | Geometry

As illustrated in Figure 1, a three-dimensional microchannel model was constructed with a width of 0.2 mm and a height of 0.067 mm. The geometry of the microchannels included variations in both bending angles and bending radii. The bending angles tested were 30°, 60°, 90°, 120° and 150°, and the bending radii were 0.1, 0.2, 0.3, 0.4, and 0.5 mm.

2.2 | Flow Field and Particle Transport Simulation

In the DPM, fluid phase is considered the continuous phase that is governed by mass continuity, momentum, and energy

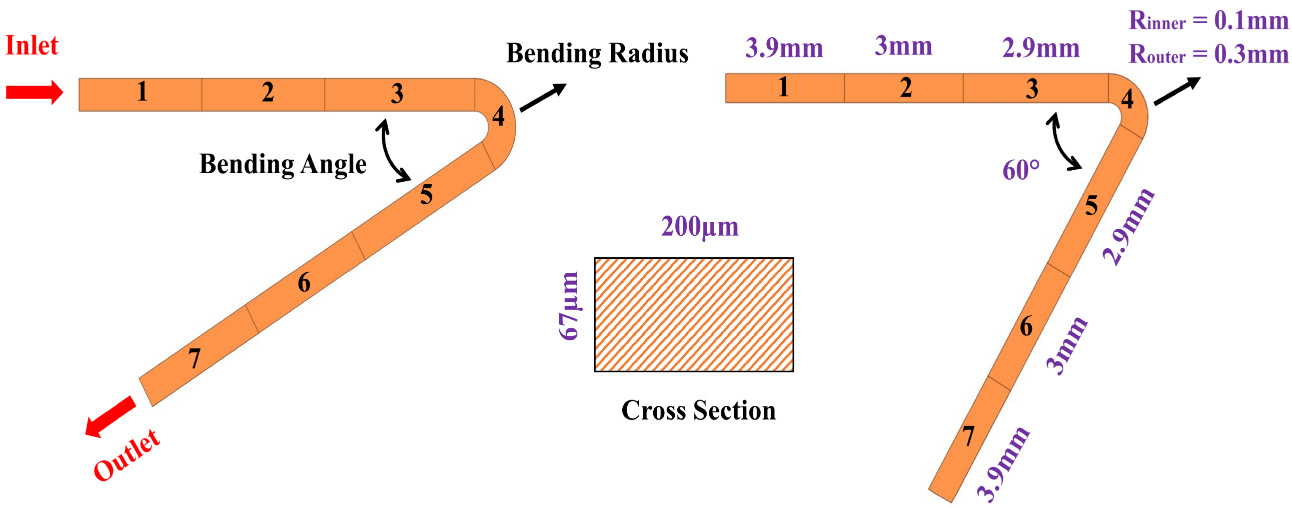

FIGURE 1 | Geometric dimensional diagram of the microchannel. [Colour figure can be viewed at wileyonlinelibrary.com]

equations, whereas the nanoparticle trajectory is calculated using Newton's Second Law, taking into account Brownian motion $\overrightarrow{F_B}$, thermophoretic force $\overrightarrow{F_T}$, gravity $\overrightarrow{F_G}$, virtual mass force $\overrightarrow{F_V}$, drag force $\overrightarrow{F_D}$, pressure gradient force $\overrightarrow{F_P}$, and Saffman's lift force $\overrightarrow{F_L}$ [22]:

$$m_p \frac{d\overrightarrow{u_B}}{dt} = \overrightarrow{F_B} + \overrightarrow{F_T} + \overrightarrow{F_G} + \overrightarrow{F_V} + \overrightarrow{F_D} + \overrightarrow{F_P} + \overrightarrow{F_L} \quad (1)$$

where m_p is the particle mass; and $\overrightarrow{u_B}$ is the particle velocity.

The amplitude of Brownian motion can be expressed as [14, 23]:

$$F_{B_i} = m_p \zeta_i \sqrt{\frac{\pi S_0}{\Delta t}} \quad (2)$$

where ζ_i is the Gaussian white noise function with a zero-mean value; Δt is the time step; and S_0 is a spectral intensity.

The thermophoretic force is formulated as [24]:

$$\overrightarrow{F_T} = -D_T \frac{\nabla T}{T} \quad (3)$$

where ∇T is the temperature difference; and D_T is the thermophoretic diffusion coefficient.

The gravitational force component is calculated by

$$\overrightarrow{F_G} = m_p \frac{\vec{g}\left(\rho_p - \rho_l\right)}{\rho_p} \quad (4)$$

The virtual mass force is calculated as [22]:

$$\overrightarrow{F_V} = C_{vm} m_p \frac{\rho}{\rho_p}\left(\overrightarrow{u_p}\nabla\vec{u} - \frac{d\overrightarrow{u_p}}{dt}\right) \quad (5)$$

The friction of the fluid can be determined by [25]:

$$\overrightarrow{F_D} = m_p \frac{\vec{u} - \overrightarrow{u_p}}{\tau_r} \quad (6)$$

where τ_r is the nanoparticle relaxation time.

The pressure gradient force is shown by [22]:

$$\overrightarrow{F_P} = m_p \frac{\rho}{\rho_p}\overrightarrow{u_p}\nabla\vec{u} \quad (7)$$

The expression for Saffman's lift force is given by [14, 26]:

$$\overrightarrow{F_L} = m_p \frac{2K\upsilon^{\frac{1}{2}}\rho d_{ij}}{\rho_p d_p \left(d_{lk} d_{kl}\right)^{\frac{1}{4}}}\left(\vec{u} - \overrightarrow{u_p}\right) \quad (8)$$

where K is the Saffman number that is taken as $K = 2.594$; and d_{ij} is the deformation tensor.

2.3 | Simulation Assumptions

In order to improve the precision and efficiency of the calculation, the following assumptions were made:

1. Nanofluid flow is three-dimensional, steady and incompressible.
2. Nanoparticles are smooth and spherical.
3. Brownian motion, thermophoretic force, gravity, virtual mass force, drag force, pressure-gradient force, and Saffman's lift force were included in the particle force balance, as described in Section 2.2. Particle-particle interactions were neglected because of the dilute nanoparticle volume fraction ($\leq 5\%$).
4. The nanoparticle distribution is uniform in the inlet.
5. Particle-wall interaction was represented using a trap boundary condition, so a particle was counted as deposited once it contacted a wall. Rebound, resuspension, adhesion-energy variation, and agglomeration after wall contact were not resolved explicitly.
6. The microchannel walls were assumed to be hydraulically smooth. Surface roughness was not included in the present model; its possible influence on near-wall collision

frequency and deposition is discussed as a limitation of the study.

2.4 | Boundary Conditions

In the simulation, the Al_2O_3-water nanofluid with a nanoparticle concentration $\varphi = 1\%$ was selected as the working fluid, and its thermophysical properties are summarized in Table 1. Al_2O_3 was selected because it is inexpensive, chemically stable, and widely used in nanofluid heat-transfer studies. A uniform inlet velocity of 0.5 m/s was prescribed, corresponding to a Reynolds number of 53.55 at 300 K. The nanoparticle concentration was also assumed to be uniform at the inlet, consistent with the dilute and well-dispersed inlet condition in Section 2.3. The outlet was modeled as a pressure-outlet. A constant heat flux of 50 kW/m^2 was applied to the top and bottom walls to represent a high-heat-flux microchannel cooling condition relevant to compact electronics and thermal management applications. The side walls were treated as adiabatic, and no-slip conditions were imposed on all walls.

2.5 | DPM Settings

To accurately capture nanoparticle deposition on the walls, the mesh was refined near the wall boundaries. The wall boundary condition was defined as a trap condition, meaning that any particle contacting the wall was considered deposited. This treatment is appropriate for evaluating relative deposition tendencies among different geometries because the present study focuses on the first particle-wall encounter and geometric control of deposition risk. The assumption is conservative, since rebound, resuspension, and surface-energy-dependent adhesion were not explicitly resolved. The dimensionless wall distance (y+) was maintained below 1 to resolve the viscous sublayer and near-wall velocity gradient, which are critical for predicting particle trajectories close to the wall and particle-wall encounter probability. Additionally, mesh density was increased near the inlet to resolve steep gradients in that region. The SIMPLE algorithm was employed with a pressure-based solver to couple pressure and velocity fields. The diffusion and convective terms in the transport equations were discretized using a second-order central difference scheme. Convergence was achieved with residuals fell below 10^{-6}.

2.6 | Grid Sensitivity Tests and Verification

In order to avoid inconsistencies in the simulation results and save computing time, a grid sensitivity test was performed. The grid sensitivity test was conducted by analyzing the velocity field, temperature field, and nanoparticle deposition rate. By varying the width, height, and length of the grid distributions, a grid sensitivity test was conducted to ensure that the model reached a grid-independent solution. Consequently, five grid combinations were used: $15 \times 50 \times 1200$, $20 \times 65 \times 1200$, $25 \times 75 \times 1200$, $25 \times 75 \times 1500$, and $25 \times 75 \times 1800$. Taking the above three aspects into account comprehensively, the grid $25 \times 75 \times 1200$ (giving the total number of mesh nodes 2,373,176) is deemed to be sufficient for the simulation, considering both accuracy and computational cost.

TABLE 1 | Specific thermophysical properties [27].

	ρ (kg/m^3)	c (J/kg·K)	k (W/mK)	μ (kg/ms)
Al_2O_3	3880	733	36	—
DI water	998.2	4182	0.587	0.000993

After the grid resolution was successfully tested, simulation validation was performed based on the flow field and nanoparticle deposition. The particle deposition model was replicated and validated against the benchmark results of Gormley and Kennedy [28] and Shi et al. [29], as shown in Figure 2, because these studies provide established reference solutions or numerical data for particle transport, Brownian diffusion, and deposition in confined tube-like flows. The purpose of this validation was to verify the DPM implementation and deposition-rate prediction rather than to reproduce the exact bent-microchannel geometry considered in the present work. The maximum relative error is only 0.15%, which is due to the Gaussian white noise (random signal) that is used to calculate the Brownian motion. Despite this, the trend remains unchanged, and the difference is also insignificant. Details can be found in our previous articles, and we have proven the model in the past [20, 21]. The model can be readily extended to account for a variety of conditions, such as different particle properties, base fluid properties, and volume fractions.

3 | Results and Discussion

This study systematically examines the effects of geometric parameters, particularly the bending angle and curvature radius, on the deposition behavior of nanoparticles within microchannels. The spatial distribution and deposition patterns of nanoparticles are analyzed to elucidate their transport and settling characteristics. These findings contribute to optimize microchannel design and enhance the understanding of nanoparticle dynamics in confined fluidic systems.

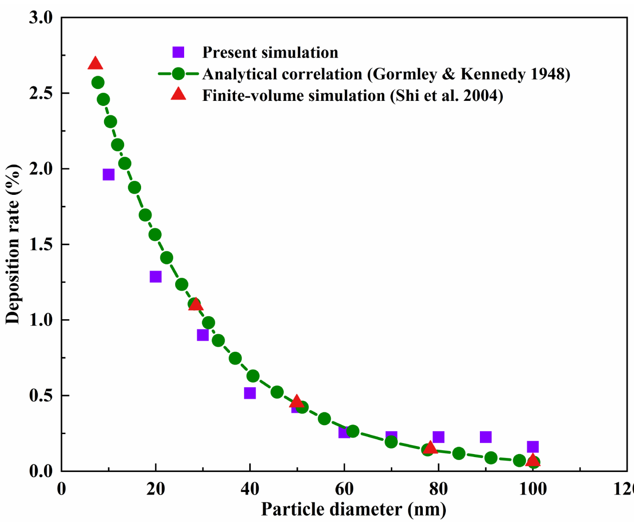

FIGURE 2 | Deposition rate changes with nanoparticle diameter [20, 21]. [Colour figure can be viewed at wileyonlinelibrary.com]

3.1 | Impact of Bending Angles on Nanoparticle Deposition

Nanoparticle deposition in microchannel cooling systems is affected by bend angle, flow rate, particle size, and nanofluid concentration. To isolate the geometric effect, only the channel bending angle was varied in this part of the study, while all other parameters were held constant. As shown in Figure 3, different bending angles lead to different particle deposition rates per unit area. Normalization by unit area is necessary because the surface area of the microchannel varies with bending angle. The results show that smaller bending angles are associated with higher particle deposition. As the channel bending angle increases from 30° to 120°, particle deposition per unit area decreases from 28.612 to 8.941. To investigate the underlying mechanism, the velocity contours within the microchannel were examined. For the bending-angle cases, the inlet velocity, hydraulic diameter, fluid properties, and curvature radius were kept constant. Therefore, the Reynolds number and Dean number remain unchanged among these cases. The bending angle does not directly change the instantaneous curvature strength represented by the Dean number; instead, it changes the streamwise length over which curvature-induced secondary flow develops and persists.

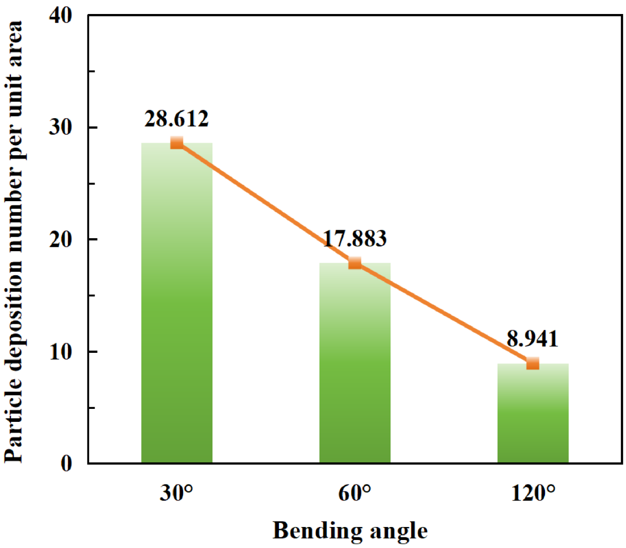

FIGURE 3 | Variation of particle deposition with bending angle. [Colour figure can be viewed at wileyonlinelibrary.com]

Figure 4 presents longitudinal cross-sectional velocity contour plots for bending angles of 30°, 60°, 90°, 120°, and 150°. The velocity contours reveal distinct low-, medium-, and high-velocity zones within the microchannel: green regions near the walls indicate low velocity, yellow regions indicate intermediate velocity, and red regions indicate high velocity. The bend produces centrifugal acceleration, creating a transverse pressure gradient and curvature-induced secondary motion. These effects change both the magnitude and direction of nanoparticle motion and increase the probability of particle-wall encounter in deposition-prone regions. However, deposition is not controlled only by the local maximum velocity. The streamwise extent of the high-velocity region, near-wall residence time, secondary-flow direction, and the position of the velocity core together determine whether particles are driven toward the wall or transported through the channel core. Therefore, the decrease in deposition at larger angles can be interpreted as the result of reduced downstream acceleration length and a redistribution of the high-velocity region, even though localized high-velocity zones become more pronounced near the bend. Changing the bending angle modifies the spatial

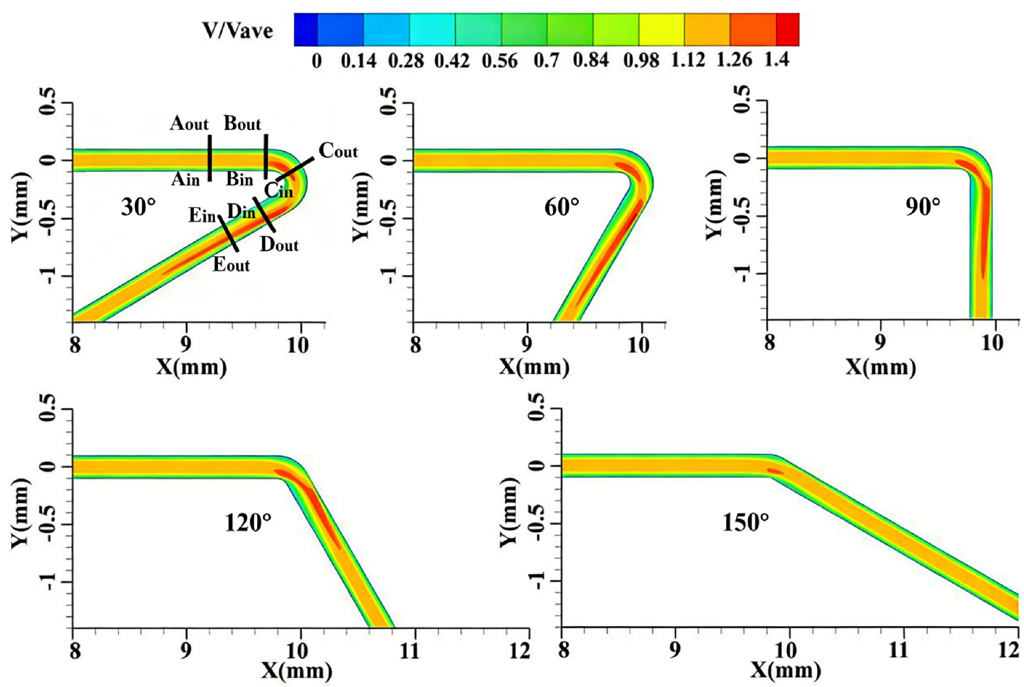

FIGURE 4 | Velocity contours along the longitudinal cross-section of microchannels at varying bending angles: (a) 30°, (b) 60°, (c) 90°, (d) 120°, and (e) 150°. [Colour figure can be viewed at wileyonlinelibrary.com]

extent and downstream persistence of the high-velocity region rather than the Dean number itself. Smaller bending angles produce a longer downstream acceleration region, increasing the distance over which particles experience curvature-induced secondary motion and near-wall migration. In contrast, at larger bending angles, such as 120° and 150°, the high-velocity region becomes more localized near the bend, reducing the downstream residence distance of particles under curvature-induced secondary flow. This explains why particle deposition decreases at larger bending angles even though localized high-velocity zones can still be observed near the bend.

A transverse cross-section velocity contour plot within the microchannel is shown in Figure 5. Five cross-sections were selected at the prebend, intrabend, and postbend locations, with extraction positions indicated by markers in Figure 4. Before the bend, the velocity contour is nearly symmetric and particle trajectories are mainly governed by the primary axial flow. As the fluid passes through the bend, centrifugal force induces secondary vortices that redistribute momentum across the channel cross-section. These secondary flows can sweep suspended particles toward the inner or outer wall, depending on the local vortex structure and pressure-gradient direction. After the bend, the high-velocity region shifts toward the outer wall, increasing particle-wall collision probability in the post-bend region. The variation of secondary vortex strength with bending angle therefore provides the physical link between the geometry-controlled velocity field and the observed deposition trend.

In a straight microchannel, the cross-sectional velocity profile is expected to be parabolic, with lower velocities near the walls and higher velocities near the center. Such a profile tends to reduce particle-wall interactions when particles remain in the core flow. In bent microchannels, the deposition rate is not a simple additive function of individual channel segments because curvature changes the local balance among inertial transport, near-wall shear, Brownian diffusion, and secondary-flow-induced transverse migration. Sharply bent regions can promote secondary vortices and local flow separation, enhancing the transport of nanoparticles toward the wall. Conversely, when the connected flow remains coherent and sufficiently fast, shear forces and core-flow transport can help keep particles suspended and reduce deposition. These mechanisms explain why the maximum velocity alone cannot predict deposition: the spatial distribution and duration of high-velocity and secondary-flow regions must also be considered.

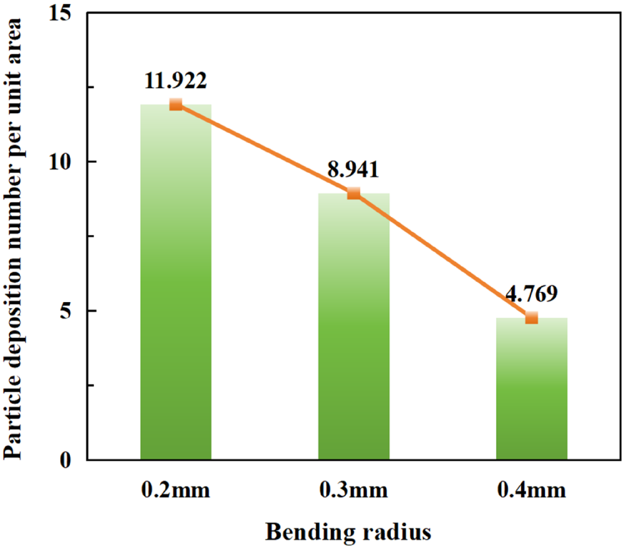

FIGURE 6 | Variation of particle deposition with bending radius. [Colour figure can be viewed at wileyonlinelibrary.com]

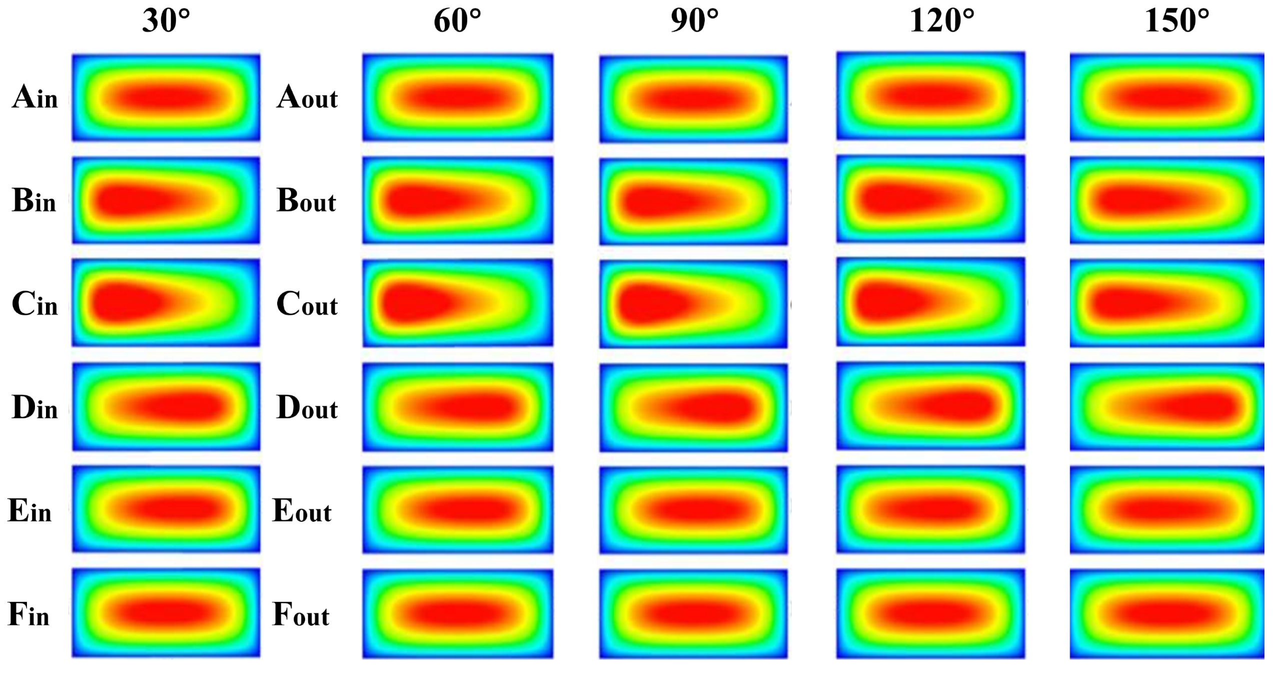

FIGURE 5 | Velocity contours across the transverse cross-section of microchannels at varying angles. [Colour figure can be viewed at wileyonlinelibrary.com]

3.2 | Effect of Bending Radii on Particle Deposition

In addition to bending angle, bending radius also influences particle deposition. Figure 6 presents a quantitative analysis of particle deposition per unit area in microchannels with varying curvature radii. Because the surface area of the curved section changes with radius, the particle deposition number is normalized by unit area to enable valid comparisons. At a bending angle of 90°, particle deposition per unit area decreases from 11.922 to 4.769 as the bending radius increases from 0.2 mm to 0.4 mm. This indicates that smaller curvature radii are more susceptible to particle deposition under the same bending angle. Mechanistically, a smaller radius strengthens curvature effects and centrifugal acceleration, which intensifies secondary flow and shifts high-velocity regions closer to the wall. As the radius increases, curvature-induced disturbance becomes weaker, the velocity core moves toward the channel center, and fewer particles are transported into near-wall collision zones. The velocity field is therefore examined to clarify how the radius controls particle trajectories and deposition.

Figure 7 illustrates longitudinal cross-sectional velocity contour plots of nanofluids in microchannels with curvature radii of 0.1, 0.2, 0.3, 0.4, and 0.5 mm. As the radius increases, the color in the bend region shifts from red to orange, indicating a decrease in the maximum velocity. The high-velocity zones also become thinner with increasing radius, suggesting weaker curvature-induced acceleration. As shown in Figure 8, transverse cross-sectional velocity contours exhibit a transition from wall-dominated flow to a more core-dominated flow: from inlet to outlet (C_{in}-C_{out}), the high-velocity region shifts away from the wall and toward the channel center. This transition reduces near-wall particle-wall encounters and helps keep particles suspended in the core flow, thereby lowering deposition. From a thermal-management perspective, radius selection should therefore be optimized jointly with heat transfer and hydraulic constraints. A larger radius may reduce deposition and wall-temperature nonuniformity, whereas excessive radius may compromise compactness; the local heat-transfer coefficient, thermal resistance, pressure drop, and wall temperature distribution should be quantified in future multiobjective design work.

3.3 | Nanoparticle Deposition Locations

Figure 9 illustrates the distribution of nanoparticle deposition counts across distinct segments of the microchannel. The microchannel is divided into seven segments, with deposition data quantified individually for each segment. To compare deposition tendencies among segments with different surface areas, deposition is normalized per unit area. The results show that the inlet region has the highest number of deposited nanoparticles compared with the other segments. Although the bent segment contains fewer total particles than the inlet segment, its smaller surface area amplifies the deposition density after normalization. This finding highlights a pronounced tendency for particle deposition to occur in curved segments. Based on the calculated

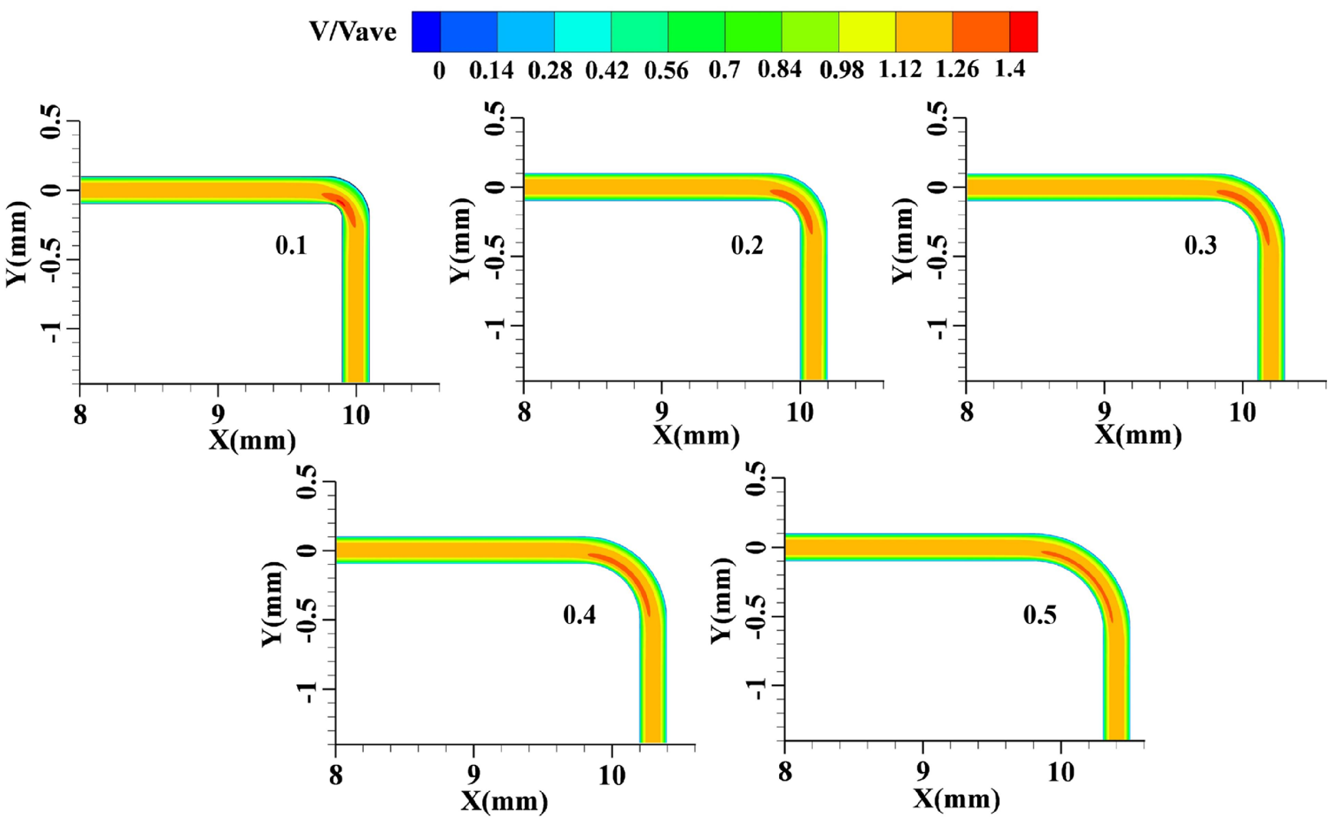

FIGURE 7 | Velocity contours along the longitudinal cross-section of microchannels at different bending radii: (a) $R = 0.1$ mm, (b) $R = 0.2$ mm, (c) $R = 0.3$ mm, (d) $R = 0.4$ mm, and (e) $R = 0.5$ mm. [Colour figure can be viewed at wileyonlinelibrary.com]

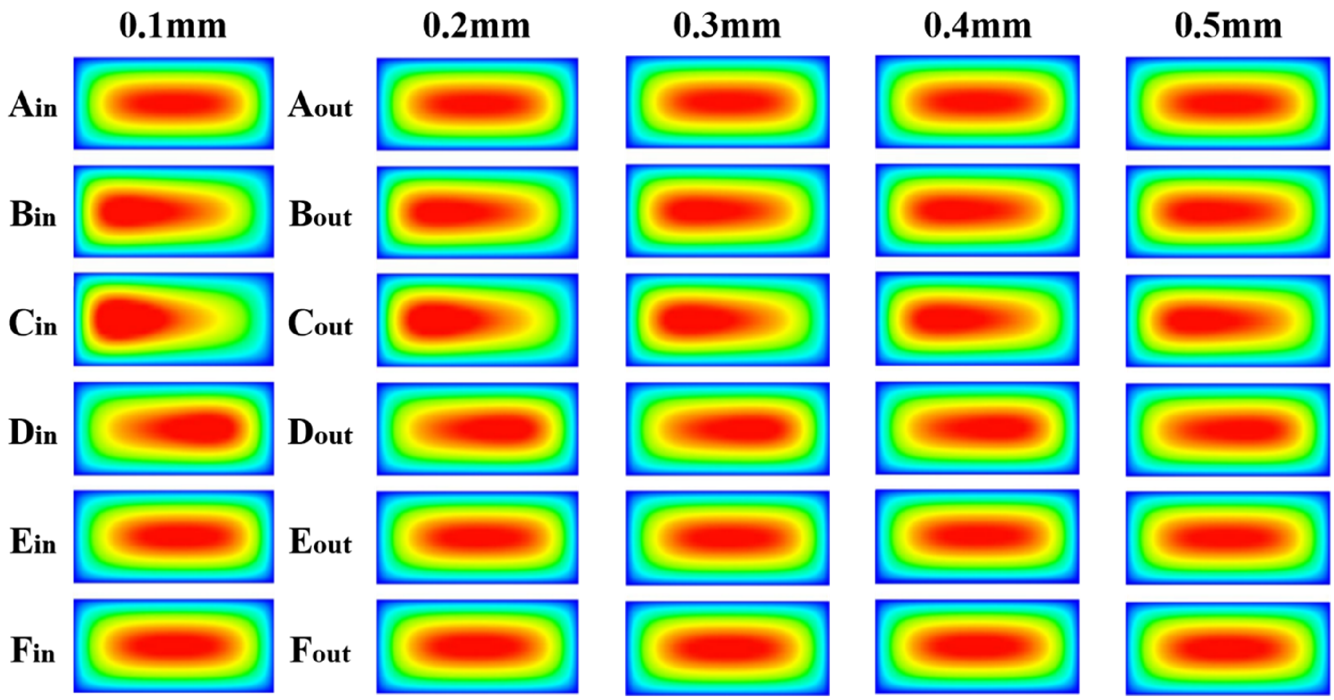

FIGURE 8 | Velocity contours across the transverse cross-section of microchannels at different bending radii. [Colour figure can be viewed at wileyonlinelibrary.com]

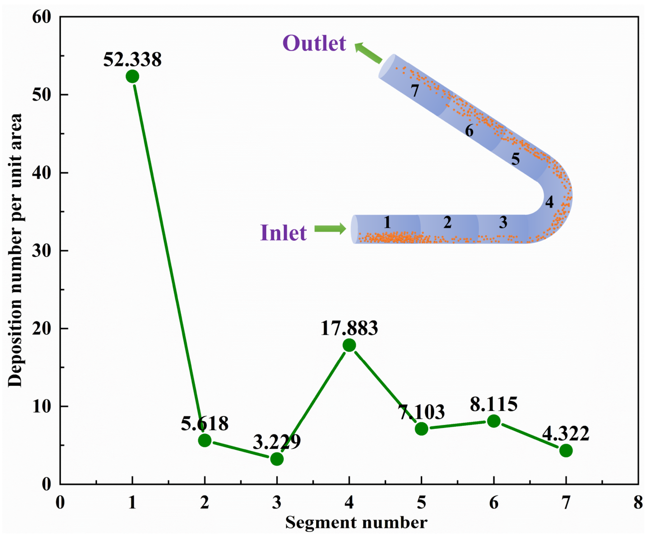

FIGURE 9 | Particle deposition number in each segment of the microchannel. [Colour figure can be viewed at wileyonlinelibrary.com]

deposition density values, the inlet and curved segments exhibit higher deposition density than the other segments.

Across all simulation segments, the majority of deposition occur at the inlet. This can be attributed to the inlet effect: upon entering the microchannel, the nanofluid experiences rapid hydrodynamic adjustment, producing immediate interactions between nanoparticles and the channel surface. The initial acceleration and developing near-wall flow increase the frequency of particle-wall collisions. Increased particle deposition in the curved segment is caused by the change in flow direction and velocity induced by the curved geometry. Flow regime, nanofluid properties, and channel geometry collectively influence deposition locations within microchannels. In practical design, inlet and bend regions should therefore be treated as priority zones for deposition mitigation, such as through inlet-flow conditioning, local surface treatment, optimized curvature, or operating-condition adjustment. A balance between reduced deposition, compactness, pressure drop, and heat-transfer performance should be considered when selecting the bending radius.

3.4 | Correlation of Nanoparticle Deposition in Bent Microchannels

To establish accurate correlations for nanoparticle deposition, the most influential factors must first be identified. This study systematically investigates the effects of geometric parameters, specifically bending angle and curvature radius, on nanoparticle deposition behavior in microchannels. Geometric optimization plays a critical role in controlling nanoparticle transport and deposition, and accurate correlations are essential for predicting nanoparticle behavior under various flow conditions and for guiding microchannel design.

Nanoparticle deposition in bent microchannels is primarily governed by the Reynolds number (Re), the Dean number (De) and deposition efficiency. Analysis of these parameters enables the prediction and optimization of deposition patterns, which is crucial for designing efficient microfluidic systems. Deposition efficiency is typically quantified by normalizing the mass of nanoparticles deposited on the channel walls by the total mass of nanoparticles flowing through the system, with consideration of the microchannel surface area.

The Reynolds number is defined as [30]:

$$Re = \frac{\rho v D_{\mathrm{h}}}{\mu} \tag{9}$$

where ρ is the fluid density, kg/m^3; v is the characteristic inlet velocity, m/s; D_{h} is the hydraulic diameter, m; and μ is the dynamic viscosity, N s/m^2.

The Dean number represents the relative strength of curvature-induced secondary flow driven by centrifugal effects, which can be expressed as [31]:

$$De = Re\sqrt{\frac{D_{\mathrm{h}}}{2R_{\mathrm{c}}}} \tag{10}$$

where R_{c} is the curvature radius of the bend, m.

The deposition rate is used to evaluate the nanoparticle deposition as [20]:

$$\eta = \frac{N_d}{N_{\mathrm{total}}} \times 100\% \tag{11}$$

where N_d is the number of nanoparticles deposited on the wall; and N_{total} is the total number of nanoparticles released from the inlet of the microchannel.

The Reynolds number directly influences the primary flow structure, while the Dean number characterizes the secondary vortices induced by channel curvature. A combined *Re-De* analysis provides a design-oriented framework for predicting nanoparticle deposition. For a given coolant, particle size, flow rate, and microchannel geometry, *Re* describes the axial transport regime, whereas De indicates the tendency for transverse secondary motion to drive particles toward the wall. Therefore, deposition-prone designs can be identified by linking *Re*, *De*, and deposition efficiency over the operating range. This framework can guide microchannel optimization by balancing deposition suppression, heat-transfer enhancement, pressure-drop penalty, and compactness. The present results provide the basis for such a correlation within the investigated geometry and Reynolds-number range; broader correlations should be developed using additional radii, angles, flow rates, particle properties, and experimental validation. It should be noted that the Dean number depends on *Re*, D_{h}, and R_{c}, but not directly on the bending angle. When these parameters are fixed, changing the bending angle mainly changes the arc length and development distance of the secondary flow, rather than the Dean number itself.

4 | Conclusion

This study investigated the effects of bending angle and curvature radius on nanoparticle deposition in microchannels. Through quantitative deposition analysis and detailed velocity-field characterization, the transport and deposition mechanisms of nanoparticles were clarified in terms of curvature-induced acceleration, secondary flow, and particle-wall encounter probability. The following conclusions can be drawn from this study:

- The particle deposition number decreases as the microchannel bending angle increases. As the channel bending angle increases from 30° to 120°, the particle deposition per unit area decreases from 28.612 to 8.941. This reduction is attributed not only to changes in local maximum velocity but also to the shortened downstream acceleration region and altered secondary-flow structure, which reduce particle residence and wall-collision probability in deposition-prone zones.
- Particle deposition decreases with increasing microchannel bending radius. Particle deposition per unit area decreases from 11.922 to 4.769 as the bending radius increases from 0.2 to 0.4 mm. A larger radius weakens curvature-induced acceleration and shifts the velocity core toward the channel center, thereby reducing near-wall particle-wall encounters.
- Based on the calculated deposition density values, the inlet and curved segments exhibit significantly higher particle deposition than the other segments. These locations should be prioritized in microchannel anti-fouling design because they are most sensitive to developing flow, directional change, and curvature-induced secondary motion.
- The Reynolds number governs the primary flow structure, while the Dean number quantifies the strength of secondary vortices induced by curvature. Together, these dimensionless parameters offer a robust basis for optimizing microchannel geometry to minimize unwanted deposition while maintaining thermal and hydraulic performance.

Future work should develop *Re-De*-deposition correlations using additional operating conditions and experimental validation. More detailed models should include wall roughness, particle agglomeration, surfactant-stabilized dispersion, rebound/resuspension, and coupled heat-transfer metrics such as local heat-transfer coefficient, pressure drop, thermal resistance, and wall-temperature distribution. These extensions would provide a more complete basis for designing nanofluid microchannel cooling systems with low deposition risk and high thermal performance.

Nomenclature

$\vec{F}$	External body forces
m	Mass
ζ_i	Gaussian white noise function
S_0	Spectral intensity
T	Temperature
v	Velocity
P	Static pressure
C_{c}	Cunningham correction
Kn	Knudsen number
d_{p}	Nanoparticle diameter
D_{T}	Thermophoretic diffusion coefficient
C_{vm}	Virtual mass factor
τ_{r}	Particle relaxation time

Re_r	Relative Reynolds number
K	Saffman number
d_{ij}	Deformation tensor
N	Deposition particle number

Greeks

ρ	Density
μ	Dynamic viscosity
ν	Kinematic viscosity
λ	Mean free path
φ	Volume concentration
β	Thermal expansion coefficient
$\overline{\tau}$	Stress tensor

Subscripts

ref	Reference
p	Particle
B	Brownian force
T	Thermophoretic force
G	Gravity
V	Virtual mass force
D	Drag force
P	Pressure gradient force
L	Saffman's lift force
nf	Nanofluids

Author Contributions

Meng Wang: conceptualization, writing – original draft, project administration, software, methodology, data curation, validation, writing – review and editing, resources. **Kai Zhang:** conceptualization, methodology, writing – original draft, visualization, validation, formal analysis, investigation. **Juanli Zhang:** methodology, writing – review and editing, formal analysis. **Jay Wang:** formal analysis, writing – review and editing, visualization, investigation.

Acknowledgments

This work is supported by the University of Glasgow. Open access publishing facilitated by Auckland University of Technology, as part of the Wiley - Auckland University of Technology agreement via the Council of Australasian University Librarians

Funding

Open access publishing facilitated by Auckland University of Technology, as part of the Wiley—Auckland University of Technology agreement via the Council of Australasian University Librarians.

Conflicts of Interest

The authors declare no conflicts of interest.

Data Availability Statement

The data that support the findings of this study are available from the corresponding author upon reasonable request.

References

1. Y. Jia, Z. Lin, J. Wang, J. Wang, and Z. Xu, "Experimental Investigation on Flow Boiling Heat Transfer Characteristics in Microchannels With Heterogeneous Modified Surfaces," *International Journal of Heat and Mass Transfer* 255 (2026): 127752.

2. F. Marzban, M. Marzban, K. Mohammadzadeh, and S. D. Farahani, "Field Synergy Analysis of Conjugate Heat Transfer in Nanofluid-Filled Wavy Microchannel Heat Sink Using DPM and DDPM Approach," *Journal of Thermal Analysis and Calorimetry* 150 (2025): 1–22.

3. Y. T. Aksoy, F. Enayati, P. Eneren, and M. R. Vetrano, "Experimental Study on Enhanced Heat Transfer via Nanoparticle Depositions Using TiO2-Water Nanofluid Sprays," *Applied Thermal Engineering* 264 (2025): 125450.

4. A. Yahyaee, P. Vatankhah, and H. Sørensen, "Effects of Nanoparticle Size on Surface Dynamics and Thermal Performance in Film Boiling of Al_2O_3 Water-Based Nanofluids," *Colloids and Surfaces A: Physicochemical and Engineering Aspects* 696 (2024): 134267.

5. M. Wang, Y. Chen, X. Li, H. Yin, M. C. Paul, and P. S. Dobson, "A Novel CFD-DPM Model for Particle Deposition and Removal in Microchannels With Different Contact Angles," *Separation and Purification Technology* 370 (2025): 133220.

6. X. Wang, Y. Song, C. Li, et al., "Nanofluids Application in Machining: A Comprehensive Review," *International Journal of Advanced Manufacturing Technology* 131 (2024): 3113–3164.

7. S. Saha, S. Raut, and A. Das, "Numerical Study of Laminar Water-Al2O3 Nanofluids Flow and Transfer of Heat Through a Rectangular Micro-Channel in Presence of Trapezoidal Baffles," *Authorea Preprints* (2024).

8. R. Steinhagen, H. Müller-Steinhagen, and K. Maani, "Problems and Costs due to Heat Exchanger Fouling in New Zealand Industries," *Heat Transfer Engineering* 14 (1993): 19–30.

9. V. Hessel, H. Löwe, and S. Hardt, *Chemical Micro Process Engineering: Fundamentals, Modelling and Reactions* (John Wiley & Sons, 2004).

10. R. L. Hartman, "Managing Solids in Microreactors for the Upstream Continuous Processing of Fine Chemicals," *Organic Process Research & Development* 16 (2012): 870–887.

11. S. Ko, J. Lee, J. Yu, D. Banerjee, and S.-W. Kang, "Nanoparticle Migration on the Microchannel Wall Surface in Low-Reynolds-Number Nanofluids," *AIP Advances* 14 (2024).

12. D. Y. Kim, S. Y. Jung, Y. J. Lee, and K. H. Ahn, "Effect of Colloidal Interactions and Hydrodynamic Stress on Particle Deposition in a Single Micropore," *Langmuir* 38 (2022): 6013–6022.

13. D. Y. Kim, S. Y. Jung, Y. J. Lee, H. Jin, and K. H. Ahn, "From Successive Deposition to Clogging of Poly (Styrene) Particles in the Cross-Flow Through a T-Shaped Microchannel," *Separation and Purification Technology* 322 (2023): 124263.

14. A. Li and G. Ahmadi, "Dispersion and Deposition of Spherical Particles From Point Sources in a Turbulent Channel Flow," *Aerosol Science and Technology* 16 (1992): 209–226.

15. W. Williams, J. Buongiorno, and L.-W. Hu, "Experimental Investigation of Turbulent Convective Heat Transfer and Pressure Loss of Alumina/Water and Zirconia/Water Nanoparticle Colloids (Nanofluids) in Horizontal Tubes," *Journal of Heat Transfer* 130 (2008): 042412.

16. Z. Han, W. Zhou, X. Zhao, and M. Zhang, "Thermal Oxidation Deposition Characteristics of RP-3 Kerosene in Serpentine Tubes Under Supercritical Pressure," *Fuel* 310 (2022): 122369.

17. X. Cong, G. Yang, J. Qu, and J. Zhao, "A Model for Evaluating the Particle Penetration Efficiency in a Ninety-Degree Bend With a Circular-Cross Section in Laminar and Turbulent Flow Regions," *Powder Technology* 305 (2017): 771–781.

18. L. H. Kumar, S. Kazi, H. Masjuki, and M. Zubir, "A Review of Recent Advances in Green Nanofluids and Their Application in Thermal Systems," *Chemical Engineering Journal* 429 (2022): 132321.

19. N. Zahari, M. Zawawi, L. Sidek, et al., "Introduction of Discrete Phase Model (DPM) in Fluid Flow: A Review," in *AIP Conference Proceedings* (AIP Publishing LLC, 2018), 20234.

20. M. Wang, P. S. Dobson, and M. C. Paul, "Numerical Investigation of Nanofluid Deposition in a Microchannel Cooling System," *Powder Technology* 425 (2023): 118582.

21. M. Wang, P. S. Dobson, and M. C. Paul, "Numerical Investigation of Nanoparticle Deposition in a Microchannel Under the Influence of Various Forces and Development of a New Correlation," *International Communications in Heat and Mass Transfer* 155 (2024): 107533.

22. *ANSYS Fluent Tutorial Guide* (ANSYS, Inc. and ANSYS Europe, Ltd., 2021).

23. W. C. Hinds, *Aerosol Technology: Properties, Behavior, and Measurement of Airborne Particles* (John Wiley & Sons, 1999).

24. L. Talbot, "Thermophoresis of Particles in a Heated Boundary Layer," *Journal of Fluid Mechanics* 101 (1979): 737–758.

25. A. Gosman and E. Loannides, "Aspects of Computer Simulation of Liquid-Fueled Combustors," *Journal of Energy* 7 (1983): 482–490.

26. P. Saffman, "The Lift on a Small Sphere in a Slow Shear Flow," *Journal of Fluid Mechanics* 22 (1965): 385–400.

27. V. Bianco, F. Chiacchio, O. Manca, and S. Nardini, "Numerical Investigation of Nanofluids Forced Convection in Circular Tubes," *Applied Thermal Engineering* 29 (2009): 3632–3642.

28. P. Gormley and M. Kennedy, "Diffusion From a Stream Flowing Through a Cylindrical Tube," *Proceedings of the Royal Irish Academy, Section A, Mathematical and Physical Sciences: JSTOR* 52 (1948): 163–169.

29. H. Shi, C. Kleinstreuer, Z. Zhang, and C. Kim, "Nanoparticle Transport and Deposition in Bifurcating Tubes With Different Inlet Conditions," *Physics of Fluids* 16 (2004): 2199–2213.

30. M. Trofa, G. D'Avino, L. Sicignano, et al., "CFD-DEM Simulations of Particulate Fouling in Microchannels," *Chemical Engineering Journal* 358 (2019): 91–100.

31. D.-B. Kwak, S. C. Kim, H. Lee, and D. Y. Pui, "Experimental Study of Nanoparticle Transport and Penetration Efficiency on a Sharp-Bent Tube (Elbow Connection)," *International Journal of Heat and Mass Transfer* 155 (2020): 119816.